Supporting Information

Unraveling the Arrangement of Al and Fe Within the Framework Explains the Magnetism of Mixed-Metal MIL-100(Al,Fe)

Gregor Mali,*[1] Matjaž Mazaj,[1] Iztok Arčon,[2,3] Darko Hanžel,[3] Denis Arčon,[3,4] Zvonko Jagličić[5]

[1] National Institute of Chemistry, Hajdrihova 19, SI-1001 Ljubljana, Slovenia

[2] University of Nova Gorica, Vipavska 13, SI-5000 Nova Gorica, Slovenia

[3] Jožef Stefan Institute, Jamova 39, SI-1000 Ljubljana, Slovenia

[4] Faculty of Mathematics and Physics, University of Ljubljana, Jadranska 19, SI-1000 Ljubljana, Slovenia

[5] Institute of Mathematics, Physics and Mechanics & Faculty of Engineering and Geodesy, University of Ljubljana, Jadranska 19, SI-1000 Ljubljana, Slovenia

*Corresponding author's email address: gregor.mali@ki.si

Synthesis of MIL-100 materials

MIL-100(Fe) was synthesized by the procedure, described by Márquez et al.,[1] with a slight modification. 0.81 g (3 mmol) of $FeCl_3 \cdot 6H_2O$ (99.9% Sigma-Aldrich) was dissolved in 10 ml of demineralized water prior to the addition of 0.28 g (1.3 mmol) of benzene-1,3,5-tricarboxylic acid (95% Sigma-Aldrich). After stirring the initial precursor solution for 5 minutes, 10 M NaOH was added dropwise to the reaction mixture until the pH of 2.5 was achieved. The final gel was transferred into 23 ml Teflon-lined autoclaves and hydrothermally treated at 150 °C for 5 days. Product was filtered, continuously washed with methanol and dried at ambient conditions.

MIL-100(Al) was synthesized according to the procedure, described by Volkringer et al.[2] 0.23 g (0.6 mmol) of $Al(NO_3)_3 \cdot 9H_2O$ (99.9% Sigma-Aldrich), 0.10 g (0.4 mmol) of benzene-1,3,5-tricarboxylate (95% Sigma-Aldrich), 0.8 ml HNO_3 (65% Merck) and 5 ml of demineralized water were mixed. Reaction mixture was transferred to Teflon-lined autoclaves and heated at 210 °C for 3.5 h. The product was isolated from mother liquour by filtration and dried at room temperature.

Mixed-metal MIL-100(Al,Fe) was synthesized along the same procedure as MIL-100(Fe), only that 0.41 g (1.5 mmol) of $FeCl_3 \cdot 6H_2O$ and 0.32 g (1.5 mmol) of $AlCl_3 \cdot 6H_2O$ were used as metal precursors.

Activation of all the prepared materials was carried out by stirring in 50 ml of methanol at 50 °C under reflux for 16 hours.

X-ray diffraction and elemental analysis

X-ray powder-diffraction data were collected on PANalytical X'Pert PRO high-resolution diffractometer with $CuK_{\alpha1}$ radiation ($\lambda = 1.5406$ Å) in the 2-theta range between 2 and 60 ° using step of 0.034 °/ 100 s. Elemental analysis was carried out on an Inductively coupled plasma mass spectrometer (ICP-MS, Agilent Technologies, Model 7900) and yielded Al/Fe ratio of 0.76 ± 0.03.

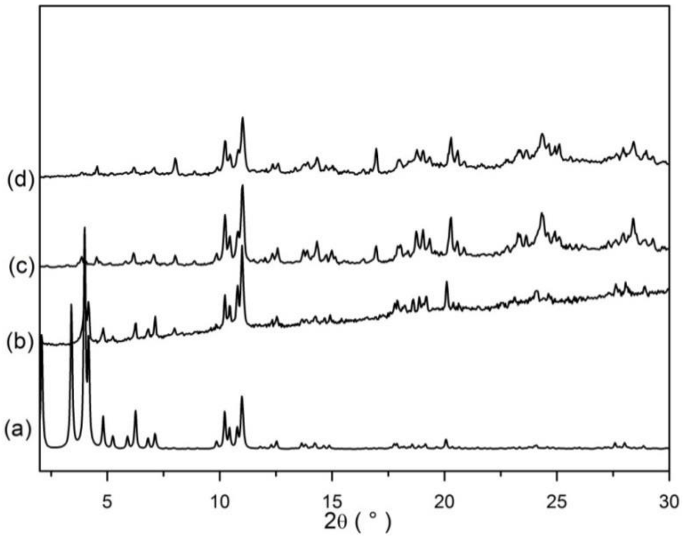

Figure S1. Calculated XRD pattern of activated MIL-100(Fe) (a), compared with the diffraction patterns of pure as-synthesized MIL-100(Fe) (b), pure MIL-100(Al) (c), and MIL-100(Al,Fe) (d) powders. Relative intensities of reflections in the measured diffractograms (particularly at low angles) differ from the calculated patterns; this is probably due to the presence of disordered water molecules within the two types of pores of MIL-100 framework, which lead to significantly different electron densities in comparison with the model with empty pores.

X-ray absorption spectroscopy

Fe K-edge XANES and EXAFS spectra of MIL-100(Fe) and MIL-100(Al,Fe) samples and Fe reference compounds (Fe_2O_3, alpha-FeOOH, Fe_3O_4, $FeSO_4$) were measured at XAFS beamline of Elettra synchrotron radiation facilities in transmission detection mode. A Si (111) double crystal monochromator was used with 0.8 eV energy resolution at 7 keV. Higher-order harmonics were effectively eliminated by detuning the monochromator crystals to 70% of the rocking curve maximum. The intensity of the monochromatic X-ray beam was measured by three consecutive 30 cm long ionization detectors respectively filled with the following gas mixtures: 580 mbar N_2 and 1420 mbar He; 90 mbar Ar, 1000 mbar N_2 and 910 mbar He; 350 mbar Ar, 1000 mbar N_2 and 650 mbar He. The absorption spectra were measured within the interval [-200 eV, 1200 eV] relative to the Fe K edge. In the XANES energy region equidistant energy steps of 0.2 eV were used, while for the EXAFS region equidistant *k* steps of 0.03 $Å^{-1}$ were adopted with an integration time of 1 s/step.

The samples and the reference Fe compounds were prepared in the form of homogenous pellets, pressed from micronized powder mixed with boronitrate (BN). In all cases the total absorption thickness of the sample was about 2 above the Fe K-edge. Sample pellets were placed between the first and second ionization cell. The exact energy calibration was established with simultaneous absorption measurement on a 5-micron thick Fe metal foil placed between the second and the third ionization chamber. Absolute energy reproducibility was ±0.01 eV.

The analysis of XANES and EXAFS spectra was performed with Demeter (IFEFFIT) program package,[3] in combination with FEFF6 program code for ab initio calculation of photoelectron scattering paths.[4]

The Fe K-edge XANES analysis was used to determine the average Fe valence state of Fe cations in the MIL-100(Fe) and MIL-100(Al,Fe) samples. The normalized XANES spectra of the samples are plotted in Figure 1A, together with a selected set of XANES spectra of standard reference Fe compounds with similar iron coordination (pure octahedral or mixed octahedral and tetrahedral coordination to oxygen ligands), and different average iron valence states between Fe^{2+} and Fe^{3+} (**Fe^{2+}**: $FeSO_4\cdot7H_2O$; **$Fe^{2.67+}$**: Fe_3O_4; **Fe^{3+}**: Fe_2O_3 (Hematite), alpha-FeOOH (Goethite)). The valence state of Fe cation in the sample can be deduced from the energy shift of the absorption edge. With increasing oxidation state each absorption feature in the XANES spectrum is shifted to higher.[5,6] A shift of the edge position of about 4.5 eV per unit oxidation state between Fe^{2+} and Fe^{3+} is observed on reference compounds (Figure 1A).

Fe XANES spectra of both samples exhibit same Fe K-edge profile and energy position. The edge position matches that in the XANES spectra of Fe^{3+} reference compounds Fe_2O_3 (Hematite) and alpha-FeOOH (Goethite) (Figure 1A) so we can deduce that average Fe valence state in both samples is 3+.

Details about the coordination of Fe cations in the MIL-100 framework can be obtained from the Fe K-edge EXAFS analysis, which can directly probe the local structure around Fe cations in the samples. Fourier transform magnitude of the Fe K-edge EXAFS spectra represents average radial distribution of neighbor atoms around Fe cation. For the two samples the EXAFS spectra are very similar (Figure 1B). Two dominant peaks are observed in the R range between 1 Å and 3.3 Å, representing the contributions of photoelectron scattering on the nearest shells of neighbors around the Fe atom. A strong peak in the R range between 1 Å and 2.2 Å can be attributed to photoelectron backscattering on the nearest oxygen neighbors around Fe. The following composed peak in the R range between 2.5 Å and 3.4 Å represents the contributions from more distant Fe coordination shells in MIL-100 crystal structure.

For quantitative Fe EXAFS analysis, a FEFF models was constructed, based on MIL-100 crystal structure,[7] where trimers of metal-oxo octahedra are linked by benzene-1,3,5-tricarboxylate anions (Schemes 1 and 2). In a single-metal MIL-100(Fe) sample Fe cations are surrounded by six oxygen atoms in a distorted octahedron, at distances from 1.85 Å to 2.05 Å, four carbon atoms distributed between 2.85 Å - 3.05 Å, four oxygen atoms at 3.29 Å to 3.37 Å, and two Fe neighbors at 3.36 Å. In a mixed-metal MIL-100(Al,Fe), where Fe and Al cations can occupy equivalent metal sites in the crystal structure, four types of metal-oxo trimers may form (3Fe, 2Fe1Al, 1Fe2Al, and 3Al trimers) (Scheme 2). So, in an average Fe local neighborhood we can expect mixed occupancy of the coordination shell at about 3.4 Å by Fe and Al neighbors. Eventual presence of fluorine atoms in Fe neighborhood cannot be tested, since in EXAFS analysis contributions of oxygen and fluorine atoms cannot be reliably distinguished due to very similar photoelectron backscattering factors and phase shifts.

The contributions of the first four Fe coordination shells in the R range from 1.0 Å to 3.4 Å (Figure 1B) were analyzed. The FEFF model comprised six single scattering paths from the nearest neighbor shells up to 3.4 Å, with three variable parameters for each type of the neighbor in each scattering path: coordination number (N), distance (R), and the Debye–Waller factor (σ^2). To detect small structural differences in the local Fe neighborhood between the MIL-100(Al,Fe) and MIL-100(Fe) samples, and to minimize uncertainties of fitting parameters due to high correlations between them in the fit of individual spectra, a parallel fit of the two spectra was performed, where some parameters were constrained to common values for both spectra and some constraints were introduced for coordination numbers of individual scattering paths. The distances and Debye–Waller factors of individual scattering paths in the two samples were constrained to common values. The shell coordination numbers were constrained to the crystallographic values, taking into account the stoichiometric values of the Fe and Al in each material. So, the coordination number of oxygen neighbors in the nearest coordination shell, distributed at two different distances, is constrained to six (octahedral coordination of Fe cations). In the same way the coordination number of Fe (or Fe and Al) neighbors in the most distant coordination shell, distributed at two slightly different distances around 3.4 Å, is constrained to two. In addition two common parameters of all scattering paths were also varied in the fits: the amplitude reduction factor S_0^2 and the shift of energy origin of the photoelectron ΔE_0. There were in total 31 independent points and 16 independent variables in the parallel fit of two spectra within the fitting range in the k interval from 3 Å^{-1} to 14 Å^{-1} and the R range of 1 Å up to 3.4 Å. A very good fit is obtained for both spectra (Figure 1B). A complete list of the best fit parameters for both samples is given in Table S1.

The results about the average local neighborhood of Fe within the MIL-100 samples agree well with the crystallographic structure data. In both samples we found 6 oxygen neighbors in the first coordination shell: five at 2.01 Å and one at 2.45 Å. Large Debye–Waller factor of the more distant oxygen neighbor indicates a weak coordinative bonding, most probably it belongs to a water molecule coordinated to Fe cation. In the second and third coordination shell we detected four carbon and four oxygen atoms at 2.99 Å and 3.24 Å, respectively. In the fourth coordination shell we identified structural difference.

In the MIL-100(Fe) sample each Fe cation has two Fe neighbors, as expected for the Fe-oxo trimer structure (Scheme 2, 3Fe trimer). The two Fe neighbors are distributed at two slightly different distances: in average there are 1.3 Fe at 3.33 Å and 0.7 Fe at 3.46 Å. The result indicates that Fe cations are positioned in the vertexes of isosceles triangle with two shorter and one longer side.

In the MIL-100(Al,Fe) sample each Fe cation has in average one Al neighbor at 3.31 Å and one Fe at 3.33 Å. The result is in agreement with the Fe/Al stoichiometry (~60% of Fe and ~40% of Al), and indicates that there are in average 2 Fe cations and one Al cation connected in each metal-oxo trimer (i.e. two Fe and one Al cations are positioned in the vertices of isosceles triangle with two shorter and one longer side). However, a mixture of three different types of metal-oxo trimers (3Fe, 2Fe1Al, 1Fe2Al) cannot be excluded (Scheme 2). The result excludes only a possibility of a simple mixture of single-metal MIL-100(Al) and MIL-100(Fe) or a composite of large Fe-rich and Al-rich domains in the sample.

Table S1. Parameters of the nearest coordination shells around Fe atoms in the MIL-100(Fe) and MIL-100(Al,Fe) samples: average number of neighbor atoms (*N*), distance (*R*), and Debye-Waller factor (σ^2). Uncertainty of the last digit is given in parentheses. The best fit is obtained with the shift of the energy origin ΔE_o = 4.9± 0.6 eV. The goodness-of-fit parameter (*R*-factor) is 0.00033.

Fe neighbor	***N***	***R* (Å)**	**σ^2(Å^2)**
MIL-100(Fe)			
O	4.9(2)	2.01(1)	0.009(1)
O	1.1	2.45(8)	0.03(1)
C	4	2.99(1)	0.008(2)
O	4	3.24(5)	0.037(6)
Fe	1.3	3.33(6)	0.011(3)
Fe	0.7	3.46(2)	0.011(3)
MIL-100(Al,Fe)			
O	5.0(2)	2.01(1)	0.009(1)
O	1.0	2.45(8)	0.03(1)
C	4	2.99(1)	0.008(2)
O	4	3.24(5)	0.037(6)
Al	1	3.31(6)	0.016(7)
Fe	1	3.33(2)	0.011(3)

Mössbauer spectroscopy

Mössbauer spectra were recorded at 297 and 4.2K using a constant acceleration Wissel spectrometer, in transmission mode with ^{57}Co source embedded in Rh matrix. Velocity calibration was performed using a thin α-Fe foil. The isomer shifts were expressed relative to α-Fe at room temperature. The spectra were fitted with the analysis code RECOIL[8] using multiplets of Lorentzian line shape. Spectra recorded at 4.2K did not show magnetic ordering An example of a low-temperature spectrum of MIL-100(Fe) is shown in Figure S2.

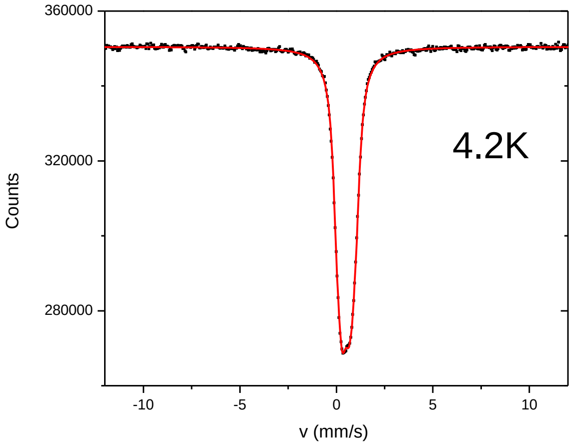

Figure S2. Mössbauer spectrum of MIL-100(Fe) recorded at 4.2 K.

EPR spectroscopy

X-band EPR spectra were recorded on a Bruker E580 spectrometer, equipped with a dielectric ring resonator ER 4118X-MD5 and Oxford cryogenics liquid He flow cryostat. The temperature stability was at all temperatures better than ± 0.1 K. In the CW EPR experiments we used microwave power of 1 mW and the modulation of field of 0.3 mT. Powder samples were placed into standard Wilmad Suprasil EPR quartz tubes with the outer diameter of 4 mm.

The measured EPR spectra were fitted with a model, in which we assumed two overlapping EPR components. For the simulations we employed EasySpin package.[9] For the component originating from the isolated Fe^{3+} (S = 5/2) centers we assumed the spin Hamiltonian that is a sum of a Zeeman and zero-field-splitting (ZFS) terms

$$H = \mu_B g_1 S \cdot B + D\left[S_z^2 + \frac{E}{D}\left(S_x^2 - S_y^2\right) - \frac{1}{3}S(S+1)\right] \quad .$$

Here μ_B is the Bohr magneton, g_1 is the isotropic g-factor of Fe^{3+} center, D is the ZFS parameter that measures the effects of axial distortion to a perfect octahedral ligand field while E is due to the rhombic distortions. The calculated powder spectrum has been broadened with the Lorentzian function with the linewidth ΔB_1. On the other hand, for the exchange-coupled signal of Fe clusters we assumed a simple Lorentzian line characterized by g_2 and the linewidth ΔB_2. For the MIL-100(Al,Fe) sample, the fit smoothly proceeded to the ZFS parameters of isolated Fe^{3+} centers with D = 0.18 cm^{-1} and E = 0.06 cm^{-1}. We note that the extracted values yield the rhombicity parameter $\lambda = E/D \approx 1/3$, which is characteristic for the distortions of Fe^{3+} octahedral environment, where the distortion is originating from the coordination complexes of Fe^{3+} and ligand molecules.[10] Interestingly, we find that for the MIL-100(Fe) ZFS parameters increase to D = 0.84 cm^{-1} and E = 0.29 cm^{-1}. The main broad components also slightly differ between the two samples. At room temperature the fits yield

g_2 = 2.09, ΔB_2 = 212 mT and g_2 = 2.02, ΔB_2 = 235 mT values for the MIL-100(Al,Fe) and MIL-100(Fe) samples, respectively. We stress that these values are not far from $g \sim 2$, typically measured in Fe^{3+} dimers in biological systems or in MOFs[11] thus corroborating our initial assignment. With decreasing temperature (e.g., measurement at 30 K), g_2 values shift to higher values, more precisely to g_2 = 2.7 in MIL-100(Al,Fe) and to g_2 = 2.45 in MIL-100(Fe). This line-shift towards lower fields is together with the loss of signal intensity fully consistent with the strong antiferromagnetic exchange interactions between Fe^{3+} moments within the Fe^{3+} clusters.

NMR spectroscopy

^{27}Al NMR spectra were recorded on a 600 MHz Varian NMR spectrometer using a 3.2 mm Varian MAS probe under static conditions. Teflon tubes, free of ^{27}Al background, were used as sample containers. ^{27}Al nuclei were excited by a soft pulse with duration of 4.5 µs. With such a pulse the whole central-transition range was irradiated. (The recorded spectrum was equal to the spectrum obtained by adding several sub-spectra, which were collected by changing the irradiation frequency in steps of 50 kHz. Practically equal spectrum was obtained also when a short hard pulse with duration of 1 µs was used for the excitation of ^{27}Al nuclei or when an echo was recorded after the application of the *soft-pulse*$-\tau-$*soft-pulse*$-\tau$ sequence.) Number of scans was 50 000. Temperature of the sample was regulated using Varian VT stack and temperature controller.

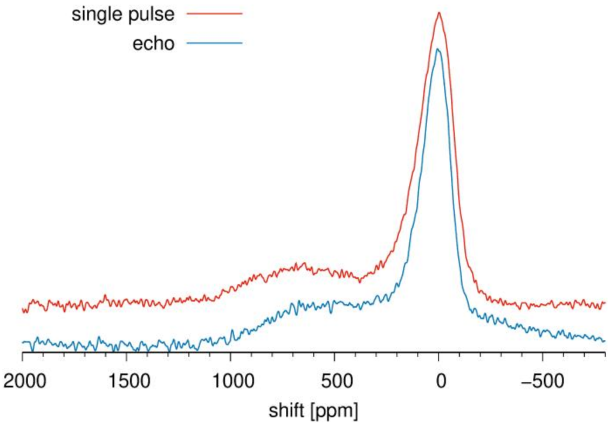

Figure S3. Static ^{27}Al NMR spectra of MIL-100(Al,Fe) recorded at 263 K, using either a single-pulse excitation or an echo sequence.

^{27}Al MAS NMR spectrum of MIL-100(Al,Fe), recorded at the sample rotation frequency of 40 kHz, was not very helpful. The broad shifted signal was not split into centerband and spinning sidebands; presumably this was because of the very short T_2 relaxation time of this contribution (see *vide infra*). One of the drawbacks of the MAS measurement was also frictional heating due to fast sample rotation. Because of this, the actual temperature of the sample during the measurement was about 320-330 K. At this temperature the overlap among different contributions to the ^{27}Al NMR spectrum is expected to be much more prominent than the overlap among these contributions at a temperature below 270 K.

The MAS NMR measurement indicates that the aluminum spectrum is composed of several contributions with centerbands in the range between -100 and 200 ppm. These contributions could belong to different Al sites within 3Al and 2Fe1Al trimers. However, in both type of trimers ^{27}Al nuclei can also exhibit different quadrupolar coupling constants, depending on the coordinating species (either water molecule or hydroxyl group). And whereas different Al sites of, for example, 3Al trimers cannot be resolved in the static ^{27}Al NMR spectrum, they probably can be distinguished in the MAS spectrum. (Similar situation is expected for the two possible coordination environments within the 2Fe1Al trimers.) Furthermore, under MAS, also satellite transitions became detectable. Altogether, MAS led to a large number of partly overlapped signals, which precluded a clearer analysis than the static ^{27}Al NMR measurement.

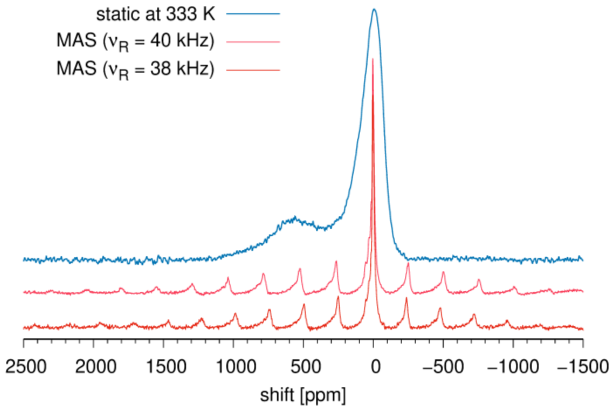

Figure S4. Comparison of ^{27}Al static and MAS NMR spectra of MIL-100(Al,Fe).

Spin-lattice relaxation measurements were carried out employing saturation recovery pulse sequence (saturation was realized by a series of 60 hard pulses, each with duration of 1 μs).[12] The obtained relaxation curves were fitted with a stretched-exponential function

$$M(t) = M_0\left(1 - e^{\left({}^{t}/_{T_1}\right)^{r}}\right).$$

For the signal with peak maximum at about 650 ppm (assigned to 1Fe2Al trimers), T_1 and r were 0.7 ms and 0.6, respectively. For the signal assigned to 2Fe1Al trimers, T_1 and r were 2.1 ms and 0.6, respectively. For the signal assigned to 3Al trimers, T_1 and r were 5.4 ms and 1, respectively. T_1 of aluminum nuclei of diamagnetic MIL-100(Al) was 228 ms.

The decomposition of the ^{27}Al NMR spectrum of MIL-100(Al,Fe) into three contributions was carried out with DMFIT software.[13] One Gaussian (for the contribution of 3Al trimers) and two static-CSA-like lines with $\eta = 0$ (for the contributions of 1Fe2Al and 2Fe1Al trimers) were used. The obtained relative intensities were corrected to account for signal losses during the instrumental dead time of 2.7 μs. To be able to do that, T_2 relaxation times were measured with a solid-echo pulse sequence. The signals resonating between -150 and 250 ppm exhibited T_2 of 120 ms and the signal with the peak maximum at 650 ppm exhibited T_2 of 15 ms. Unlike the T_1 relaxation times, T_2 relaxation times of the 2Fe1Al and 3Al contributions were too similar to allow the distinction of the two contributions.

Measurements of magnetic susceptibility

Magnetic properties were investigated by a Quantum Design MPMS-XL-5 SQUID magnetometer using polycrystalline samples. Magnetization *M* was measured between 2 K and 300 K in three magnetic fields ($\mu_0 H$ = 0.1, 1, and 5 T) and the susceptibility was calculated as $\chi = M/H$. Above 20 K the susceptibility is independent of the magnetic field *H*, and $\chi(T)$ curves superimpose confirming a linear dependence of magnetization versus magnetic field up to 5 T. Only below 20 K the susceptibilities measured in different magnetic fields separate.

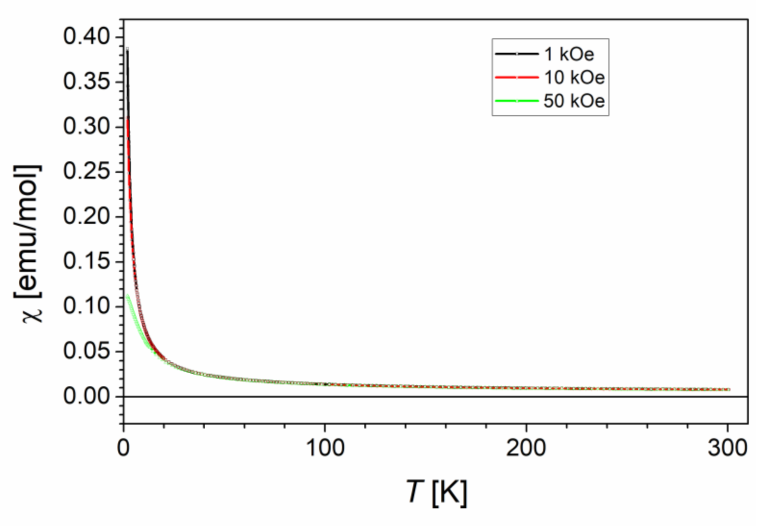

Figure S5. Magnetic susceptibility of MIL-100(Al,Fe) as a function of temperature, measured at three different magnetic fields.

The temperature dependence of the magnetic susceptibility of MIL-100(Al,Fe) does not follow the Curie or Curie-Weiss expression. This is because the material comprises contributions of different types of metal-oxo trimers. In 1Fe2Al trimers, Fe^{3+} cations do behave as independent paramagnetic centers. As opposed to that, the DFT-based calculations predict strong antiferromagnetic coupling between Fe^{3+} centers in 2Fe1Al and 3Fe trimers. The expected temperature dependence of magnetic susceptibility for a set of coupled pairs of Fe^{3+} ions (given by expression (3) in the main text) is compared to the temperature dependence of magnetic susceptibility of independent paramagnetic centers (as given by the Curie law (1) in the main text) in Figure S4.

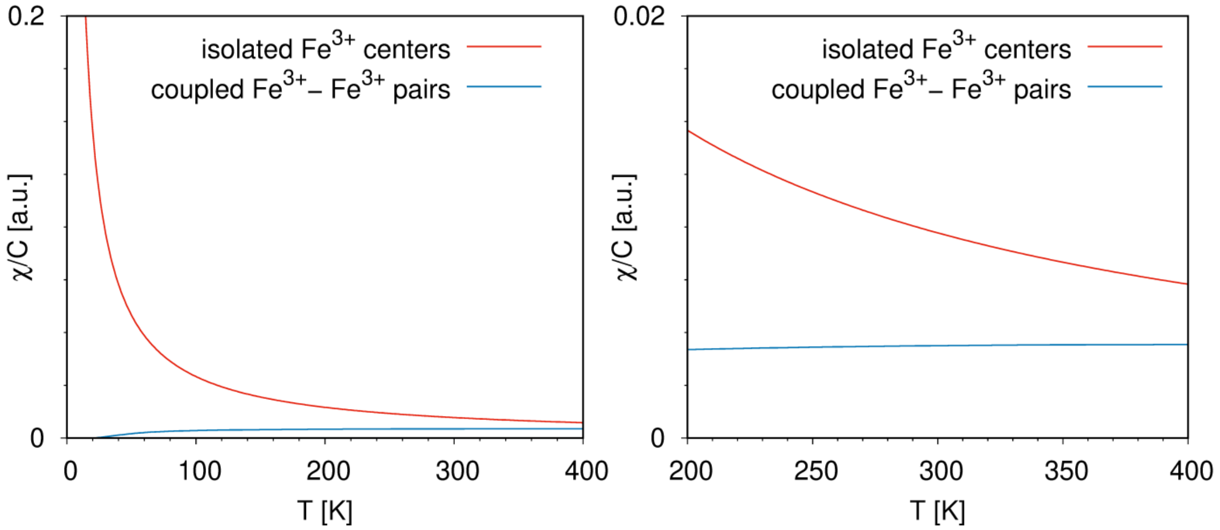

Figure S6. Comparison of magnetic susceptibilities calculated for isolated spins with S=5/2 and for coupled pairs of spins with S=5/2. For the latter, magnetic susceptibility was calculated with expression (3), which assumes that coupling can be described by the Heisenberg Hamiltonian $H = -2J\vec{S}_1 \cdot \vec{S}_2$, and takes $J = -6\,meV$. $C = Ng^2\mu_B^2/k$.

Computation

First-principles calculations of hyperfine coupling and spin-spin coupling constants were carried out with Orca 4.0.1.2 package. The DFT-based calculations were performed at PBE0-D3/def2-QZVPP level. The hybrid PBE0 exchange-correlation functional, incorporating 25% Hartree-Fock exchange, was selected, because it has been demonstrated on several different examples to yield accurate hyperfine coupling constants (e.g. in Li*TM*PO4 materials with *TM* = Mn, Fe, Co, and Ni,[14] and in Ni, Co, and Cr organic complexes[15]) and because this functional is generally available in various computational packages. The def2-QZVPP basis set is also a generally available basis set that offers enough flexibility in the region of core electrons to lead to converged calculations of the hyperfine coupling tensors. To confirm the adequacy of this basis set, results of calculations with the def2-QZVPP basis set were compared also to results of calculations with a specialized aug-cc-pVTZ-J basis set and with denser grids on metal centers. (The aug-cc-pVTZ-J basis was specifically developed for accurate calculations of hyperfine coupling constants.[16,17]) Hyperfine coupling constants A_{HF} and spin-spin coupling constant J obtained with the two different approaches agreed to within 5-10 %.

Prior to the calculation of hyperfine coupling constants A_{HF} and the evaluation of the spin-spin coupling constant J, molecular clusters, representing various instances of 3Fe, 2Fe1Al, 1Fe2Al, and 3Al trimers, were geometry optimized. Ground state energies of the optimized clusters are compared in Figure S7. In the figure,

$$\Delta E_{\mathrm{Al}_n\mathrm{Fe}_{3-n}} = E_{\mathrm{Al}_n\mathrm{Fe}_{3-n}} - \frac{nE_{\mathrm{Al}_3}}{3} - \frac{(3-n)E_{\mathrm{Fe}_3}}{3},$$

and $E_{\mathrm{Al}_n\mathrm{Fe}_{3-n}}$, E_{Al_3}, E_{Fe_3} are the energies of the (3-*n*)Fe*n*Al, 3Al and 3Fe trimers, respectively.

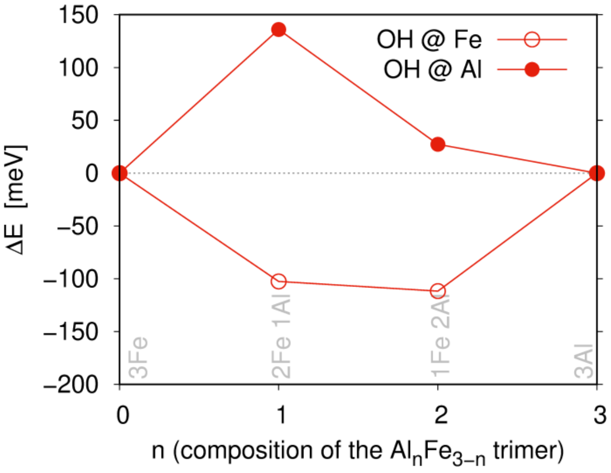

Figure S7. Ground-state energies (convex hull) for the various geometry-optimized metal-oxo trimers. The energies depend not only on the Al/Fe composition of the trimers, but also on the coordination of Al or Fe with OH^- or H_2O. Each metal-oxo trimer comprises two water molecules and one hydroxyl group.

Spin-spin coupling constant for the 2Fe1Al trimer was calculated as

$$J = \frac{E_{\mathrm{HS}} - E_{\mathrm{BS}}}{\langle S^2 \rangle_{\mathrm{HS}} - \langle S^2 \rangle_{\mathrm{BS}}}$$

where HS and BS denote the high-spin-state and broken-symmetry-state quantities (energy and expectation value of the total spin of the cluster).[18]

References

(1) Márquez, A. G.; Demessence, A.; Platero-Prats, A. E.; Heurtaux, D.; Horcajada, P.; Serre, C.; Chang, J.-S.; Férey, G.; Peña-O'Shea, V. A. de la; Boissière, C.; et al. Green Microwave Synthesis of MIL-100(Al, Cr, Fe) Nanoparticles for Thin-Film Elaboration. *Eur. J. Inorg. Chem.* **2012**, *2012* (32), 5165–5174.

(2) Volkringer, C.; Popov, D.; Loiseau, T.; Férey, G.; Burghammer, M.; Riekel, C.; Haouas, M.; Taulelle, F. Synthesis, Single-Crystal X-Ray Microdiffraction, and NMR Characterizations of the Giant Pore Metal-Organic Framework Aluminum Trimesate MIL-100. *Chem. Mater.* **2009**, *21* (24), 5695–5697.

(3) Ravel, B.; Newville, M. ATHENA, ARTEMIS, HEPHAESTUS: Data Analysis for X-Ray Absorption Spectroscopy Using IFEFFIT. *J. Synchrotron Radiat.* **2005**, *12* (4), 537–541.

(4) Rehr, J. J.; Albers, R. C.; Zabinsky, S. I. High-Order Multiple-Scattering Calculations of x-Ray-Absorption Fine Structure. *Phys. Rev. Lett.* **1992**, *69* (23), 3397–3400.

(5) Arčon, I.; Kolar, J.; Kodre, A.; Hanžel, D.; Strlič, M. XANES Analysis of Fe Valence in Iron Gall Inks. *X-Ray Spectrom.* **2007**, *36* (3), 199–205.

(6) Dominko, R.; Sirisopanaporn, C.; Masquelier, C.; Hanzel, D.; Arcon, I.; Gaberscek, M. On the Origin of the Electrochemical Capacity of Li2Fe0.8Mn0.2SiO4. *J. Electrochem. Soc.* **2010**, *157* (12), A1309–A1316.

(7) Férey, G.; Serre, C.; Mellot-Draznieks, C.; Millange, F.; Surblé, S.; Dutour, J.; Margiolaki, I. A Hybrid Solid with Giant Pores Prepared by a Combination of Targeted Chemistry, Simulation, and Powder Diffraction. *Angew. Chem. Int. Ed.* **2004**, *43* (46), 6296–6301.

(8) Lagarec, K.; Rancourt, D. G. *RECOIL Mössbauer Spectral Analysis Software for Windows*; Department of Physics, University of Ottawa, 1998.

(9) Stoll, S.; Schweiger, A. EasySpin, a Comprehensive Software Package for Spectral Simulation and Analysis in EPR. *J. Magn. Reson.* **2006**, *178* (1), 42–55.

(10) Klencsár, Z.; Köntös, Z. EPR Analysis of Fe3+ and Mn2+ Complexation Sites in Fulvic Acid Extracted from Lignite. *J. Phys. Chem. A* **2018**, *122* (12), 3190–3203.

(11) Osadchii, D. Y.; Olivos-Suarez, A. I.; Szécsényi, Á.; Li, G.; Nasalevich, M. A.; Dugulan, I. A.; Crespo, P. S.; Hensen, E. J. M.; Veber, S. L.; Fedin, M. V.; et al. Isolated Fe Sites in Metal Organic Frameworks Catalyze the Direct Conversion of Methane to Methanol. *ACS Catal.* **2018**, *8* (6), 5542–5548.

(12) Yesinowski, J. P. Finding the True Spin–Lattice Relaxation Time for Half-Integral Nuclei with Non-Zero Quadrupole Couplings. *J. Magn. Reson.* **2015**, *252*, 135–144.

(13) Massiot, D.; Fayon, F.; Capron, M.; King, I.; Calvé, S. L.; Alonso, B.; Durand, J.-O.; Bujoli, B.; Gan, Z.; Hoatson, G. Modelling One- and Two-Dimensional Solid-State NMR Spectra. *Magn. Reson. Chem.* **2002**, *40* (1), 70–76.

(14) Pigliapochi, R.; Pell, A. J.; Seymour, I. D.; Grey, C. P.; Ceresoli, D.; Kaupp, M. DFT Investigation of the Effect of Spin-Orbit Coupling on the NMR Shifts in Paramagnetic Solids. *Phys. Rev. B* **2017**, *95* (5), 054412.

(15) Vaara, J.; Rouf, S. A.; Mareš, J. Magnetic Couplings in the Chemical Shift of Paramagnetic NMR. *J. Chem. Theory Comput.* **2015**, *11* (10), 4840–4849.

(16) Provasi, P. F.; Sauer, S. P. A. Optimized Basis Sets for the Calculation of Indirect Nuclear Spin-Spin Coupling Constants Involving the Atoms B, Al, Si, P, and Cl. *J. Chem. Phys.* **2010**, *133* (5), 054308.

(17) Hedegård, E. D.; Kongsted, J.; Sauer, S. P. A. Optimized Basis Sets for Calculation of Electron Paramagnetic Resonance Hyperfine Coupling Constants: Aug-Cc-PVTZ-J for the 3d Atoms Sc–Zn. *J. Chem. Theory Comput.* **2011**, *7* (12), 4077–4087.

(18) Soda, T.; Kitagawa, Y.; Onishi, T.; Takano, Y.; Shigeta, Y.; Nagao, H.; Yoshioka, Y.; Yamaguchi, K. Ab Initio Computations of Effective Exchange Integrals for H–H, H–He–H and Mn2O2 Complex: Comparison of Broken-Symmetry Approaches. *Chem. Phys. Lett.* **2000**, *319* (3), 223–230.